Producing photoactive, transparent and hydrophobic SiO$_2$-crystalline TiO$_2$ nanocomposites at ambient conditions with application as self-cleaning coatings

Chrysi Kapridaki [a], Luís Pinho [b], Maria J. Mosquera [b,**], Pagona Maravelaki-Kalaitzaki [a,*]

[a] School of Architectural Engineering, Technical University of Crete, Akrotiri University Campus, 73100 Chania, Crete, Greece
[b] TEP-243 Nanomaterials Group, Departamento de Química-Física, Facultad de Ciencias, Campus Universitario Río San Pedro, Universidad de Cádiz, 11510 Puerto Real, Cádiz, Spain

ABSTRACT

Nowadays, the enhancement of atmospheric pollution is dramatically increasing the presence of soiling on buildings in every city of the world. Thus, the development of photocatalysts as self-cleaning coatings is a promising challenge. The first object of this work was to develop a simple synthesis route for obtaining SiO$_2$-crystalline TiO$_2$ nanocomposites at ambient temperature. Thus, it meets the requirements to produce photoactive coatings on buildings and, additionally, it can be used in other applications requiring low temperature. The second objective was to gain insights into the structure of these materials and to establish the relationship between their structure and their performance as photocatalysts.

The synthesis process involves mixing titanium and silicon alkoxides in the presence of oxalic acid. An organic silica oligomer is also added to reduce surface energy and consequently, to give hydrophobic properties to the material. These products were applied as a coating on marble specimens in order to investigate their effectiveness. The results obtained highlight that oxalic acid acts a chelating agent of the titanium precursor, giving rise to a homogeneous TiO$_2$–SiO$_2$ material. In addition and most importantly, oxalic acid produces photoactive anatase crystals at ambient temperature. From our investigation on the structure of these materials, we conclude that the formation of independent domains of TiO$_2$ inside of SiO$_2$ matrix, and the anatase crystal size are key factors for improving the photoactivity of the coatings. We also conclude that the oxalic acid concentration plays a crucial role in the formation of this optimum structure.

© 2014 Elsevier B.V. All rights reserved.

1. Introduction

Atmospheric pollution is dramatically increasing the external decay of buildings in every city of the world. One of the most visible signs of decay is the presence of ugly black crusts on large exposed areas of buildings, due to the deposition of organic matter and other contaminants. Hence, the development of self-cleaning coatings, using TiO$_2$ as a photocatalyst, has received special attention from researchers in recent years [1].

In the case of building materials based on cement or lime (concretes, mortars, etc.), TiO$_2$ has been successfully mixed with the bulk material during the manufacturing processes, giving photocatalytic properties and, as an additional benefit, improving the mechanical properties of materials [1–3]. In the specific case of lime mortars, TiO$_2$ has also enhanced carbonation of the lime and the formation of hydraulic faces [3].

When the self-cleaning product needs to be applied on the external surface of existing buildings or on previously formed materials, such as stones, tiles or plasters, there are serious restrictions to the synthesis process, because the product is applied, in situ, under outdoor conditions [4–6]. Thus, the process needs to consist of an extremely simple, one-step synthesis route, with no requirement for any additional operation, such as heating, in the actual application of the product. Another limitation for these products is that the energy required for scaled-up production should be minimized.

In the literature, there are only a few references to TiO$_2$-based products applied to buildings. Specifically, TiO$_2$ nanoparticles have been previously applied to the external surface of building materials by dispersion in water [7,8] and combined with acrylic polymer

* Corresponding author. Tel.: +30 2821037661; fax: +30 2821037841.
** Corresponding author. Tel.: +34 956 016331; fax: +34 956 016288.
E-mail addresses: ckapridaki@gmail.com (C. Kapridaki), luis.pinho@uca.es (L. Pinho), mariajesus.mosquera@uca.es (M.J. Mosquera), pmaravelaki@isc.tuc.gr (P. Maravelaki-Kalaitzaki).

in various commercial products [9], and even as titanium isopropoxide sol [10]. The main drawback of these strategies is that these coatings are easily removed from the building surfaces [4,7]. An alternative approach for producing long-term coatings is to incorporate TiO_2 nanoparticles in a starting sol containing silica oligomers and *n*-octylamine [4]. The resulting crack-free mesoporous SiO_2 matrix, incorporating TiO_2 particles, adheres well to building substrates.

Another possible means of incorporating TiO_2 within a SiO_2 matrix could be by mixing Ti and Si alkoxide precursors. Thus, the sol would have a lower viscosity than that of the previously described sol containing titania particles, facilitating its deeper penetration into the building material. However, this route presents the following limitations in the actual application, especially under outdoor conditions exposed to the weather: (1) Ti alkoxides hydrolyze much faster than Si alkoxides [11], so the coating produced on the building material could lack homogeneity; (2) the formation of photoactive TiO_2 crystals commonly requires high temperatures [12].

In a previous paper, our research group investigated the possibilities of mixing Ti and Si alkoxides for producing self-cleaning coatings on stones [13]. Specifically, we prepared a starting sol by mixing tetraethoxysilane and titanium (IV) isopropoxide in the presence of oxalic acid at ambient temperature. Polydimethylsiloxane was added in order to reduce the coating surface energy and consequently, to give hydrophobic properties to the material [14,15]. We obtained crack-free, homogeneous, transparent, photoactive TiO_2–SiO_2 composites at ambient temperature. An important additional finding is that the material synthesized, when applied on marble stone by a simple spraying process, gave self-cleaning properties to the stone. We also thought oxalic acid could have reacted with calcium carbonate from marble, producing calcium oxalate, which is more stable and resistant to weathering [16,17]. From the results obtained, we concluded that oxalic acid played two roles: (1) it promoted the simultaneous transition of the TEOS and TTIP since a homogeneous gel is created; and (2) gel cracking was prevented due to its effect as a drying control chemical additive (DCCA) [18].

In accordance with our previous conclusions about the critical role played by oxalic acid in the final properties of these photoactive composites, the first objective of the work reported here is to optimize the previously devised synthesis route by significantly increasing the oxalic acid concentration. In order to investigate the effect of the content of oxalic acid on the properties of the composite, we prepared two materials with different oxalic acid concentration. In a preliminary test, we have observed that TEOS gelled instantaneously in the presence of water and oxalic acid employed as a catalyst. Thus, we decided that the TEOS should be added in the last step of the synthesis process. Furthermore, we investigated the effect of oxalic acid content and the modification of the reaction steps on its photocatalytic effectiveness. For comparison purposes, we also tested the TiO_2–SiO_2 composite synthesized in Ref. [13].

The second objective of this work was to gain insights into the structure of these materials and to establish the relationship between their structure and their performance as photocatalysts. Specifically, we employed several techniques, including TEM/STEM, AFM and nitrogen physisorption, to investigate their textural parameters such as gel network architecture, TiO_2/SiO_2 packing, surface area and pore volume. In particular, we also focused our attention on the crystallinity of TiO_2 since this parameter is intimately related to the photoactivity of the synthesized materials.

Finally, we paid attention to the role that oxalic acid ions could play a role as a hole-scavenger according the literature [19–22] by the following reasons: (1) they are good bidentate ligands (2) at low

Table 1
Composition and gelation time of the sols under study.

Material	$H_2C_2O_4$ moles[a]	Gelation time (days)	
		Open vessel	Closed vessel
STP-1	0.0001	5	35
STP-2	0.017	9	45
STP-4	0.036	5	7

[a] Referenced to 1 mol TEOS.

pH values, they are absorbed on the positively charged surfaces of TiO_2; (3) oxalic acid ions firstly bind photogenerated holes and secondly are oxidized; (4) new reactive radicals are produced through the former process, thus increasing the photoactivity.

2. Experimental procedure

2.1. Synthesis

SiO_2–TiO_2 composites were prepared by using tetraethyl orthosilicate (TEOS, Sigma Aldrich), titanium (IV) isopropoxide (TTIP, Sigma Aldrich) and hydroxyl-terminated polydimethylsiloxane (PDMS, Sigma Aldrich), as raw materials. Ethanol (EtOH, Sigma Aldrich), isopropanol (ISP, Merck) and de-ionized water were used as solvents, while oxalic acid dihydrate (Ox, Panreac) was used as a catalyst. In order to evaluate the effect of oxalic acid on the final properties of the composites, we prepared two formulations with different Ox concentration.

The synthesis of the new nanocomposites, denoted as STP-2 and STP-4 (initial letters of silica, titania and PDMS, respectively) is presented in Fig. 1. This route comprises the following steps: (a) PDMS, EtOH, H_2O and Ox were stirred at room temperature using magnetic stir bars for 90 min; (b) TTIP diluted with EtOH was added into the previous solution, drop by drop, providing a solution of two phases (c), which was subjected to further magnetic stirring for 24 h. Particularly for the synthesis of STP-2, the addition of TTIP should be completed within 4 h at the most, thus preventing particle agglomeration [23]. Finally, TEOS was also added to the previous solution and a transparent sol was obtained (d).

For purposes of comparison we also synthesized the previously described TiO_2–SiO_2–PDMS composite; details of the synthesis of that composite are given in our earlier paper [13]. This material was named STP-1 given its lower oxalic acid concentration (see Table 1). The STP-2 and STP-4 nanocomposites have a molar ratio of TEOS/EtOH/H_2O/PDMS/TTIP equal to 1/5.6/4/0.04/0.017, whereas for the STP-1 nanocomposite, this ratio is 1/4/4/0.04/0.017.

After the synthesis, the sols under study were each cast into a transparent mold the top of which was sealed by a moldable film (Parafilm). In the open vessel, the film was perforated in order to simulate the treated stone structure. The molds were kept under laboratory conditions to dry and were monitored for cracking by visual inspection.

2.2. Sol–gel characterization

Fourier Transform Infrared Spectroscopy (FTIR) using a Perkin-Elmer 1000 spectrometer in the spectral range of 400–4000 cm^{-1} was used to characterize both the sols and the xerogels. Details of the FTIR procedures employed can be found in the Supplementary Information (S1.1). The sol spectra were recorded at various stages during the synthesis, as follows: (a) the sol of PDMS–EtOH–Ox after being left to react for up to 90 min (Fig. 1a); (b) the sol that is obtained after the addition of TTIP to the sol (a) in two time intervals, immediately (b_1) and after 24 h (b_2); and (c) after the addition of TEOS to sol (b) (Fig. 1c). Spectra were also recorded for the xerogels of the three nanocomposites under study.
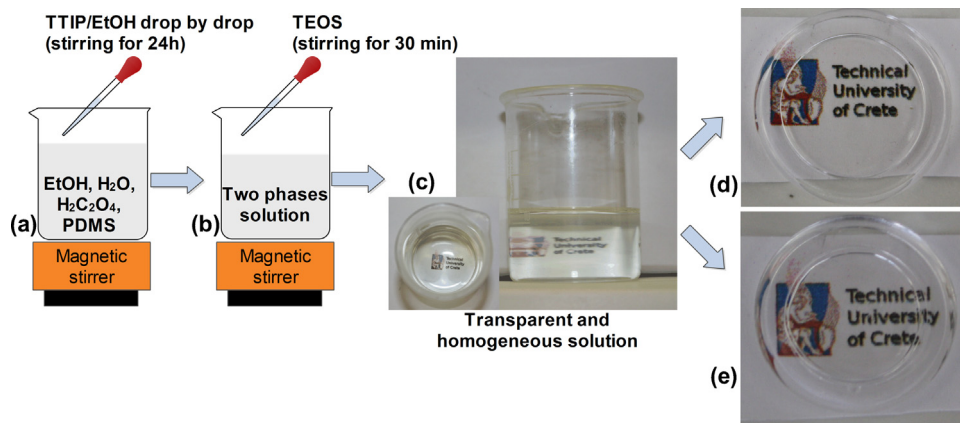
Fig. 1. (a–c) Typical experimental procedure for the synthesis; (d and e) photographs of the STP-2 and STP-4 xerogels obtained under drying at laboratory conditions, respectively.

The thermal decomposition of the nanocomposite coatings was analyzed by means of differential thermal analysis (DTA) and thermogravimetric (TG) analysis with a Setaram LabSysEvo 1600. The TG analysis was performed under N_2 atmosphere at a heating rate of 10 °C/min from 27 to 1000 °C. Prior to the experiment, the samples were dried at 60 °C for 1 day.

Textural characterization was performed by N_2 physisorption at 77 K, using a Quantachrome Autosorb IQ. The isotherms obtained were used to calculate pore volume and BET surface area of the powdered nanomaterials. The adsorption data were analyzed using a hybrid NLDFT (non-local density functional theory) approach that allows quantification of both micro- and meso-pores [24]. The hybrid NLDFT method also allows the calculation of the pore size distribution of materials containing pores of different geometry.

Transmission electron microscopy studies were performed in a JEOL 2010F TEM/STEM microscope, operating at 200 kV with 0.19 nm spatial resolution. This instrument is equipped with a JEOL high angle annular dark field (HAADF) detector and an Oxford X-Max Silicon Drift X-Ray Energy Dispersive Spectroscopy (XEDS) detector, enabling the acquisition of STEM images and compositional analysis either by spot mode or elemental mapping using a 0.5 nm electron probe. Samples were prepared by depositing a small amount of the powders directly onto Lacey-Carbon coated Cu grids. Images were obtained in TEM and STEM–HAADF modes.

The crystallinity of the nanocomposites was studied by X-ray diffraction (XRD) using a Burker D8 Advance diffractometer, operated at 35 kV and 35 mA with Cu Kα radiation with a nickel filter at a scan rate of 2° min^{-1} and a Bruker Lynx Eye strip silicon detector.

The surface of the nanocomposites was also investigated using atomic force microscopy (AFM, Nanotec Electrónica S.L.) operated in tapping mode. Roughness measurements were performed on 1 μm × 1 μm scans.

Finally, diffuse reflectance spectra (DRS) of the three nanocomposites under study were recorded in the range of 200–800 nm by using a Varian Cary 3 spectrometer equipped with an integrating sphere. All the spectra were transformed to a magnitude proportional to the extinction coefficient through the Kubelka–Munk function, $F(R)$. For comparative purposes, we have also tested commercial TiO_2 nanoparticles (P25) from Evonik.

2.3. Photocatalytic activity of the nanocomposites

The photocatalytic activity of the nanocomposites under study was investigated by evaluating the photocatalytic degradation of methyl orange (MO, Fluka). Additional information on these experiments can be found in the Supplementary Information (S1.2). For comparison purposes, we also tested the photoactivity for the degradation of MO from: (a) TiO_2-P25, as a reference photocatalyst; (b) TiO_2 obtained from TTIP at ambient conditions; and (c) the previous TiO_2 formulation in the presence of Ox. All the experiments were performed in a UV chamber equipped with four 8 W black light blue lamps, emitting in the near-UV range (315–400 nm; 3 mW cm^{-2}). The volume of the photoreactor was 25 mL.

The results obtained showed a good fit by non-linear regression, considering that the photocatalytic degradation of MO follows a pseudo-first order kinetic model. Therefore, the kinetic behavior of the photocatalysts can be ascribed according to the following equation:

$$C = C_0 e^{-kt}, \tag{1}$$

where C corresponds to MO concentration at various time intervals; k is the pseudo first order kinetic constant; t is the reaction time; and C_0 is the initial MO concentration ($t = 0$).

Through this specific type of fitting, the values of k as well as the values of the respective regression coefficients (r^2) were obtained [25].

2.4. Application and characterization of the coatings on marbles

The sols under study were applied on previously shaped and polished Greek marbles from Naxos, which are widely used in historic and modern building constructions. Specific details of application are described in the additional information (see S1.3). After constant weight was reached, the treated samples and their untreated counterparts were then investigated using the procedures described below.

The capillary water absorption capacity and the water contact angle values were measured and evaluated to characterize the effectiveness of the materials in providing hydrophobic protection. The capillary water absorption capacity was measured using the gravimetric sorption technique, according to the UNI-EN 15801:2010 [26]. The results were plotted as the mass of absorbed water per area of sample versus the square root of time. The slope obtained is denoted the capillary coefficient.

The water contact angle measurements were made using an optical tension meter (Thetalite TL 101, KSV) under laboratory conditions, according to the sessile drop method. Specific details of the procedure are described in Ref. [27].

Water vapor permeability was also performed on special disk-shaped specimens, according to UNI-EN 15803:2010 [28]. The marble discs (5 cm in diameter and 2 cm in height) were fixed on the top of a home-designed PVC unit containing 30 mL of water for measurement of permeability. The results were plotted as the mass of water vapor permeability per unit of surface versus time; the

curve defines the water vapor permeability, which was calculated as the slope of the linear curve.

To estimate color changes of the treated marbles the chromatic parameters and the total color difference (ΔE^*) were obtained by reflectance using a spectrophotometer (Konica Minolta, CM2600d) [29].

The photocatalytic activity of the nanocomposites was also evaluated by observing the discoloration of Methylene Blue (MB, Panreac) applied on the marble specimens. Specifically, 1 mL of a solution of 1 mM MB dissolved in ethanol was deposited on the treated and untreated marbles. The colored specimens were later irradiated in the UV chamber. The photocatalytic activity of the treated marbles is presented through the ratio of $\Delta E^*/\Delta E_0^*$ at various irradiation times, where ΔE_0^* expresses the total color difference between treated MB stained and treated unstained surface at time equal to 0 min. ΔE^* corresponds to the same measurements recorded at each irradiation time.

3. Results

3.1. Sol–gel characterization

The sol–gel transition took place spontaneously. The results indicate that the sequence of the reagents and their amounts again determine the gelation time. Therefore, real comparisons can be only made between STP-2 and STP-4, which clearly indicate that shorter gelation times are obtained for a higher Ox content (see Table 1). This confirms the role of Ox as a sol–gel catalyst (see Table 1). In the case of STP-1, the time taken to gel is shorter than that corresponding to STP-2 because TEOS is added in the first step of the synthesis, and this material takes a longer time to produce sol–gel transition.

We obtained crack-free, colorless, homogeneous and highly transparent nanocomposites (see Fig. 1d and e). Firstly, we consider it significant that the amount of Ti alkoxide added to the starting sols, at a slow rate of addition, was low enough to ensure a high degree of transparency for the nanocomposites obtained.

Secondly, as is well-known [30], an inherent difficulty when synthesizing Si and Ti alkoxides is to obtain homogeneous gels, because of their different reaction rates, as a consequence of the difference in the electronic partial charge on the two metal atoms. In the synthesis process presented here, it is thought that Ox facilitates the creation of homogeneous gels in the following ways: (1) the oxalate ion is a strong ligand and is coordinated with the Ti alkoxide, thus delaying the Ti alkoxide hydrolysis process [30,31]; (2) it also acts as a catalyst of the TEOS sol–gel transition [13,32]; and (3) Ox prevents the agglomeration of TiO$_2$ particles by modifying the pH of the medium [32].

The role of Ox as chelating agent also provides an explanation of the differences in gelling time between STP-2 and STP-4. Since the TTIP concentration is the same in both materials, it is thought that not all of the Ox which is present in STP-4 acts as a chelating agent. Thus, there is a surplus available for TEOS catalysis, shortening the gelling time of the material (see Table 1).

Finally, we would also point out that crack-free coatings are obtained thanks to the presence of: (1) Ox, which acts as a drying control chemical additive (DCCA) [18]; and (2) PDMS, which gives toughness and flexibility to the gel network. These contribute to preventing gel cracking during drying [14,15].

In order to gain further insights into the sol–gel process we employed the FTIR technique. Spectra of the STP-4 sol at different reaction time and STP-1, STP-2 and STP-4 xerogels spectra were recorded (see Fig. 2). The spectra tracking the evolution of the STP-2 sol with similar profiles can be checked in the supplementary information (Fig. S2).
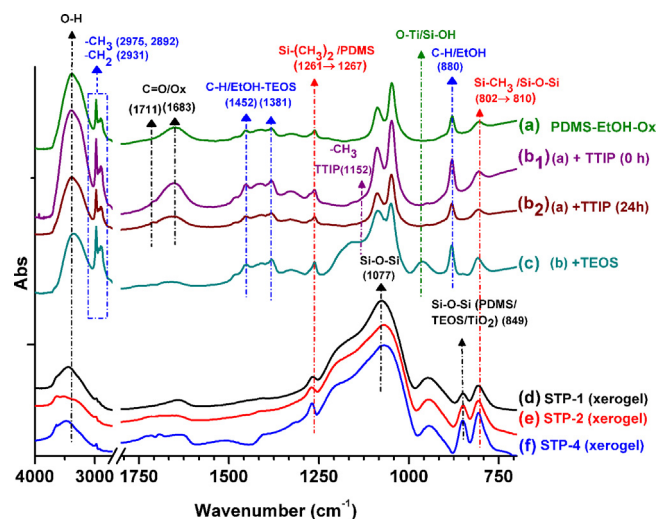

Fig. 2. FTIR spectra of the synthesized nanocomposite STP-4 sol–gel at various time intervals: (a) the PDMS–EtOH–Ox mixture reacted for up to 90 min; (b1) immediately after the addition of TTIP; (b2) 24 h after the addition of TTIP; (c) after the addition of TEOS; (d) STP-1 xerogel; (e) STP-2 xerogel; and (f) STP-4 xerogel.

The spectra of the sols under study (Fig. 2) showed a wide band attributed to the O—H stretching from the absorbed water and ethanol. As expected, this band decreased over time [13]. Regarding the reagents, the O—H band is also present in the PDMS spectra because it is a hydroxyl-terminated oligomer. In the case of the two alkoxides, O—H is present in TTIP and it is absent in TEOS. It confirms that TTIP presents higher reactivity, as previously discussed [30], because it is partially hydrolyzed.

As expected, the C—H absorptions of —CH$_2$/—CH$_3$ [13], which are present at the initial time, have decreased in spectra (d)–(f) of the three xerogels (see Fig. 2), as a consequence of the hydrolysis of the alkoxides. These characteristic peaks for C—H are also seen in the spectra of TEOS, PDMS and EtOH (Fig. S1) [33].

It should be noted that the peak observed at 1683 cm^{-1} in the initial spectrum (a), corresponding to C=O stretching vibration of Ox, showed a 'shoulder' at 1711 cm^{-1} after the addition of TTIP, seen in spectra (b1) and (b2). We think that this appearance could be associated with a possible coordination between the oxalate ligand and the Ti alkoxide added, thus preventing the instantaneous TTIP hydrolysis and polymerization [34]. This demonstrates the role of Ox as a chelating agent.

The characteristic peak of the symmetrical bending of the —CH$_3$ groups in Si—(CH$_3$)$_2$ is clearly observed in the PDMS spectrum at 1261 cm^{-1} (see Fig. S1) [14]. This peak is also present for all the reaction times (Fig. 2), indicating the integration of PDMS into the gel network. It is thus assumed that this organic component provides hydrophobic properties to the final materials.

Further, in the spectra (b1) and (b2) (Fig. 2) the addition of TTIP is confirmed by the presence of two peaks previously observed in the TTIP spectrum (Fig. S1). Specifically, there are two 'shoulders' at 945 and 1152 cm^{-1}, which can be attributed to O—Ti and —CH$_3$, respectively [35].

In the spectrum (c) the presence of TEOS is confirmed by an increase in the intensity at 945 cm^{-1} attributed to Si—OH. As time passed, the hydrolysis of TEOS and the co-polymerization of the nanocomposite can be confirmed by observing the changes of various absorptions in the spectra (d)–(f) (Fig. 2) of the xerogels STP-1, STP-2 and STP-4, respectively. Specifically, the presence of a peak at 1077 cm^{-1} can be explained by the non-symmetrical stretching of the newly created Si—O—Si bonds seen in spectra (d)–(f).
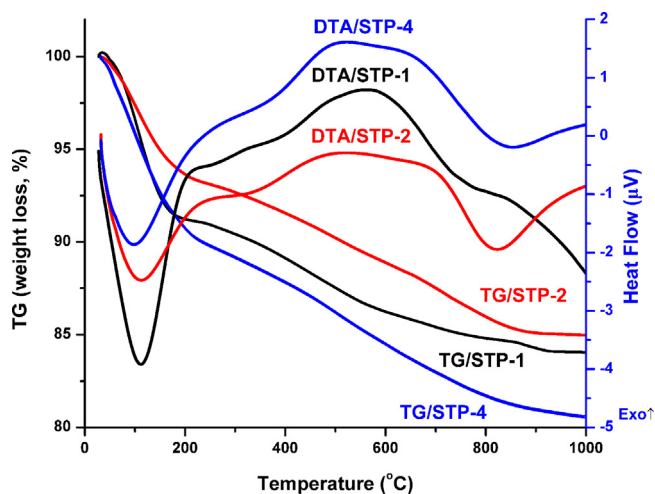
Fig. 3. DTA and TG curves of the nanocomposites under study.

Furthermore, in the spectra of the xerogels (d–f in Fig. 2), the characteristic peak of PDMS molecules at 1261 cm^{-1} is seen to have shifted to a higher wavenumber (1267 cm^{-1}); this finding, together with the appearance of a new peak at 849 cm^{-1}, whose intensity increases with time, is probably associated with the copolymerization of PDMS with TEOS [13].

All the above findings from the FTIR analysis confirm the occurrence of both the completion of the hydrolysis of TEOS and the copolymerization of TiO$_2$ and PDMS within the silica network, giving rise to the formation of a homogeneous hybrid xerogel.

Fig. 3 illustrates the TG–DTA results for the three nanocomposites prepared in our laboratory. The weight losses after heating from 40 to 205 °C were of 9, 10 and 7%, for STP-1, STP-2 and STP-4, respectively. These weight reductions, denoted by an endothermic peak, correspond to the absorbed water. A further weight loss (of 7% for STP-1, 8% for STP-2 and 10% for STP-4) was observed at higher temperatures (up to 950 °C), and is associated with the decomposition of organic components [36]. This demonstrates that the organic component was integrated into the gel network during the sol–gel transition. Thus, organic–inorganic hybrid nanocomposites were obtained.

In order to investigate the textural properties of the nanocomposites under study, nitrogen adsorption–desorption isotherms were obtained, which are shown in Fig. 4. The corresponding text-

Fig. 4. Nitrogen adsorption–desorption isotherms for the nanocomposites under study. NLDFT pore size distributions are shown as an insert.

Table 2
Textural parameters obtained from the isotherms and the NLDFT method for the materials under study.

	S_{area} (m^2/g)	V_{pore} (cm^3/g)
STP-1	153	0.136
STP-2	3	0.006
STP-4	440	0.260

ural data obtained are given in Table 2. In the case of STP-2, the pore volume and surface area values were significantly lower than those obtained for the other materials. Thus, the pore size distribution could not be obtained. This behavior is considered in greater detail in the TEM discussion included in following paragraphs.

The isotherms are type IV, which is typical of mesoporous materials. The three materials under study showed a type H4 hysteresis loop, characterized by parallel and almost horizontal branches. As Kruk and Jaroniec reported [37], type H4 loops may be associated with materials composed of particles with internal voids of irregular shape and broad size distribution. The H4 loop could also arise from the presence of large mesopores embedded in a matrix with pores of much smaller size.

Regarding the pore size, the two materials showed adsorption at low pressure, which is indicative of the existence of microporosity [12]. Therefore, we employed the NLDFT approach in order to obtain a pore size distribution covering both micro and mesopores [24]. The inset included in Fig. 4 shows the pore size distribution obtained using the isotherm adsorption branches.

Fig. 5 shows representative images of the three materials under study. Images a–c were obtained using TEM and images d, e and f correspond to HAADF–STEM images. The X-EDS spectra obtained, showing elemental distributions for Ti, Si and Si + Ti over the spots highlighted on the HAADF–STEM images, are shown in the supplementary information (Fig. S3).

The TEM images show significant differences between STP-1 and the other materials under study. STP-1 presents a uniform SiO$_2$-TiO$_2$-PDMS network composed of aggregates ranging 40–100 nm, confirming that a good Ti-O-Si connectivity, at atomic level, is achieved [38]. This obviously demonstrates that the Ti and Si precursors do not create independent domains. In the case of the materials with the highest Ox concentration (STP-2 and STP-4), we observe a matrix composed of aggregates of size similar to those shown in STP-1. However, in these cases, nanoparticles, presumably of TiO$_2$, incorporated within the SiO$_2$ matrix, can be observed. This information is in good agreement with the previous observations of Gopal et al. [39] and suggests that Si and Ti could be in separate domains. By comparing STP-2 and STP-4, significant differences in particle sizes and amounts can be clearly detected. The highest Ox concentration (STP-4) produces the particles of smallest size, ranging from 2 to 5 nm, indicated by yellow arrows in Fig. 5c. The particles in STP-2 are larger (5–10 nm) and the amount of particles is significantly greater, producing TiO$_2$ aggregates inside the SiO$_2$ matrix. Thus, these particles are more difficult to discern in the TEM images (Fig. 5b). This difference in particle size suggests that the crystal lattice could be larger for STP-2 than for STP-4. Regarding the differences in the amount of particles, this finding indicates that a higher TiO$_2$ content is present in separate domains for STP-2.

The existence of a significantly larger amount of TiO$_2$ particles and their aggregation in the STP-2 xerogel provides an explanation of its reduced pore volume and subsequent low surface area values observed by physisorption. Concretely, we think this high aggregation of TiO$_2$ crystalline particles, which does not contain pores, produces a dramatic decrease in the pore volume and subsequent surface area of the composite. This feature has previously been confirmed for composites containing SiO$_2$ non-porous particles
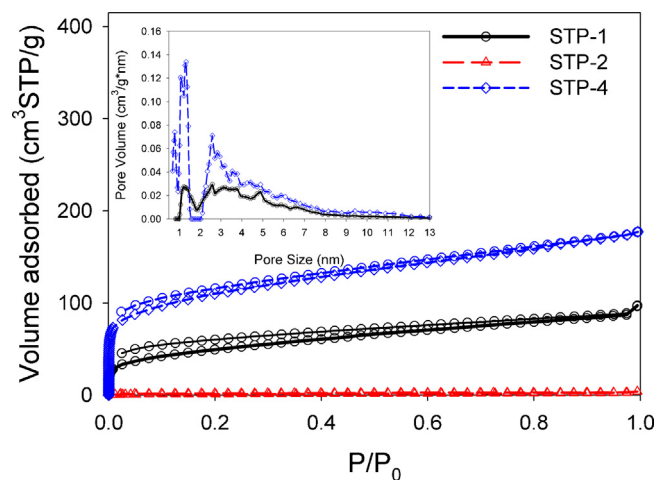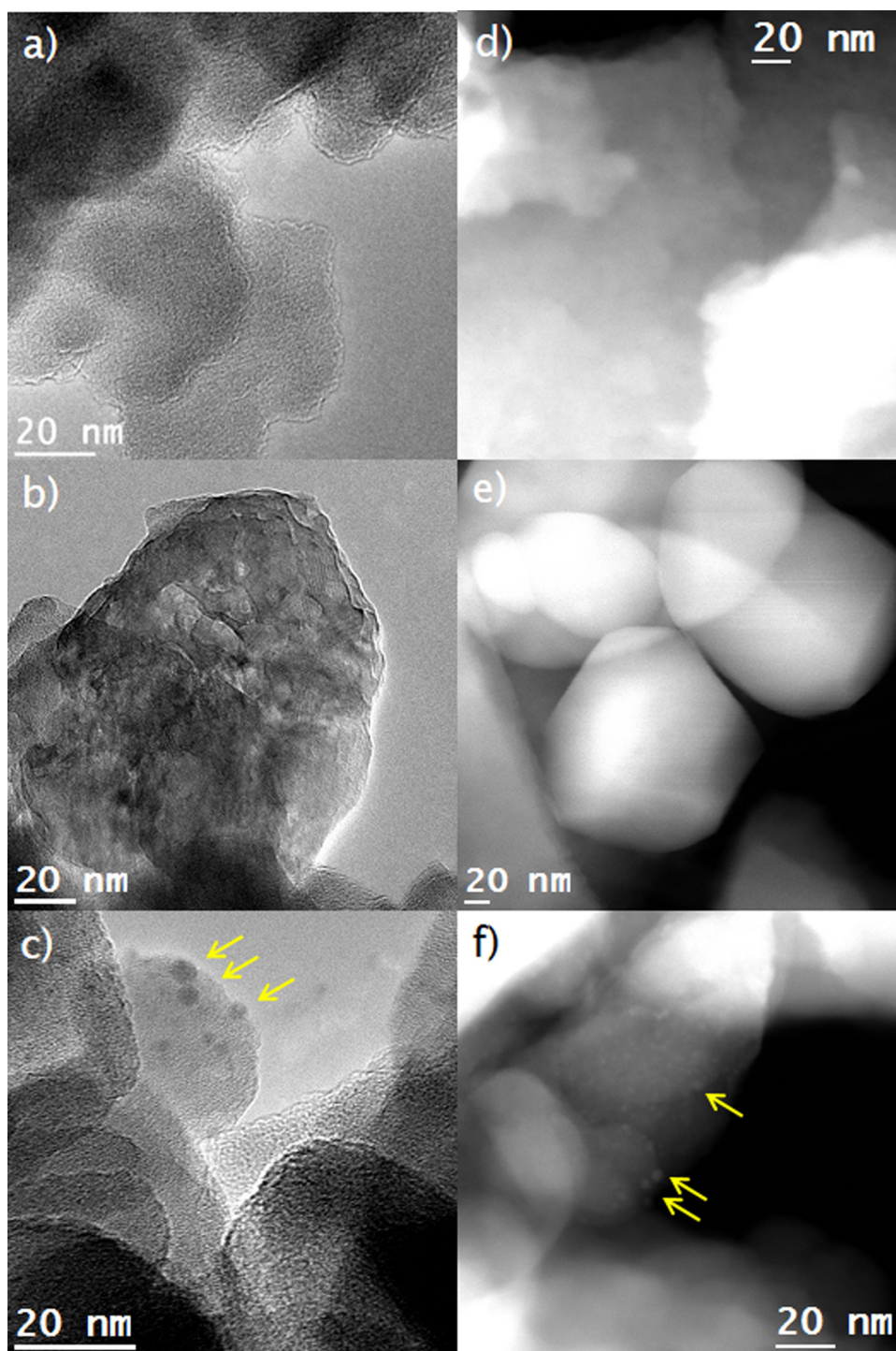
Fig. 5. (a–c) TEM images and (d–f) STEM–HAADF images for STP-1, STP-2 and STP-4, respectively.

[27]. As the particles content was increased, the pore volume of the material was reduced. This hypothesis is corroborated by the observation of the TEM images obtained (see Fig. 5a–c), STP-1 and STP-4 show a light texture (pores can be observed) whereas the STP-2 texture is dense (without pores).

The HAADF–STEM images for the materials under study (see Fig. 5d–f) provide contrast sensitive to compositional changes and allows identification of components in the nanocomposite materials [40]. The images obtained confirm the previous discussion. Firstly, Fig. 5d does not present any difference in contrast across the material, confirming that STP-1 presents connectivity at the

atomic level [38]. Unlike this, however, the materials with higher Ox concentration (Fig. 5e and f) do show a visible contrast between particles and matrix. We observe differences in contrast in the two materials. Specifically, STP-2 shows zones with higher contrast which could correspond to TiO_2 particles with a higher atomic number than that associated with the SiO_2 matrix. From this image it is possible to elucidate the presence of independent TiO_2 domains, which are hardly observed at all in the TEM mode. In STP-4, smaller and spherical TiO_2 domains are observed (they are indicated by yellow arrows in Fig. 5f), confirming the findings from the previous discussion of the TEM images.
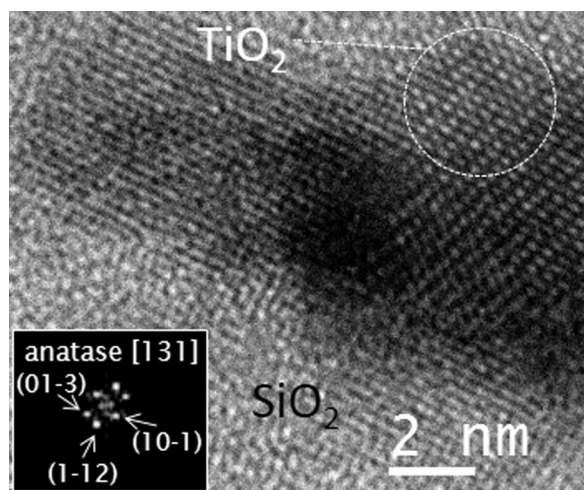
Fig. 6. HREM image corresponding to the STP-2 nanocomposite. The structural analysis of this image confirms the presence of anatase in the TiO$_2$ nanoparticles which are present in the STP-2 material.

In order to confirm the Si and Ti distribution in the materials under study, we obtained X-EDS spectra (shown in supplementary information, Fig. S3). In the case of STP-1, Si is clearly detected but the Ti peaks are not observed on the three spots analyzed (Fig. S3a). We think the reason could be the homogeneous distribution of Ti precursor, at the atomic level, in the material, which produces a very low concentration of Ti across the material, not detected by the analyzer.

For STP-2 (Fig. S3b), we analyzed spots in three zones presenting different intensity signals. Ti is not detected in the spot with lower intensity (Fig. S3b, spot b1) whereas it is clearly observed in the other two spots. This confirms that higher contrast zones correspond to independent domains of TiO$_2$, as previously discussed. By comparing b2 and b3 spots, we can confirm that the higher Ti peaks correspond to the spot with the highest contrast (b3).

Finally, the signals for STP-4 (Fig. S3c) confirm the previous discussion. In this case, we can even discern individual particles presenting higher contrast than that corresponding to the matrix. The analysis of these particles confirms the presence of Ti.

In order to obtain further insights into the structure of the materials with separate domains (STP-2 and STP-4), we have obtained HREM images (High Resolution Electron Microscopy). In Fig. 6 (corresponding to STP-2), TiO$_2$ nanoparticles with an estimated size of 5 nm can be observed supported in a silica matrix. This feature again illustrates that TiO$_2$ generates a separate domain inside the matrix. Since STP-4 showed a similar structure, the corresponding figure has not been included. The darker zones in the image could correspond to the overlapping of at least two crystalline particles. Again, it should be noted that TiO$_2$ nanoparticles are more difficult to observe because they are embedded within the silica matrix and thus, the zone under observation is less transparent to the electron beam.

The HREM image (Fig. 6) illustrates an important feature with respect to the structure of TiO$_2$ in these materials: the alkoxide precursor produces crystalline structures within the silica matrix, in the presence of oxalic acid, at ambient temperature. Specifically, from analyzing their digital diffraction patterns (shown as an inset in Fig. 6), we can confirm the crystallographic nature of the components inside our materials. The application of Fourier transformation to the visible lattice spacing present in the crystalline structure of our materials reveals the presence of $(0\,1\,-3)$, $(1\,0\,-1)$, $(1\,-1\,2)$ crystallographic planes assigned to the anatase phase of TiO$_2$. This confirms that anatase, the crystalline structure

of TiO$_2$ presenting higher photoactivity, is present in our materials. As expected, the silica matrix is an amorphous structure.

Since the crystallographic nature of TiO$_2$ is detected by HREM, we obtained X-ray diffractograms for the materials under study. They are shown in the supplementary information (Fig. S4). No diffraction peaks corresponding to TiO$_2$ crystalline phases (anatase, rutile or brookite) are detected. Similarly, Bonne et al. [41] hardly detect anatase by XRD whereas they do observe these crystalline structures by TEM. We think that the small size and the lack of orientation observed in the crystalline network could be responsible for the absence of XRD crystalline peaks.

From the TEM and physisorption studies reported in the preceding paragraphs it is possible to draw conclusions about the texture and the microstructure of the materials under study. Firstly, in respect of the distribution of Si and Ti, the significant difference between STP-1 and the other two materials could be associated with the different sequence for the addition of the reagents. In the synthesis of STP-1, TEOS is added in the first step, and is hydrolyzed prior to the addition of TTIP. We think that this first step promotes hetero-condensation of Si and Ti, producing Ti—O—Si connectivity at the atomic level. In contrast, for the synthesis of STP-2 and STP-4, TEOS is added in the last step. Thus, TTIP homo-condensation takes place prior to the addition of TEOS and subsequently, the separate TiO$_2$ domains are created inside the silica network.

Secondly, in STP-2 and STP-4, the formation of anatase crystals at ambient temperature can be associated with a peptization process occurring during synthesis. As previously reported [42,43] the addition of acid re-disperses amorphous TiO$_2$ particles (peptization). It greatly facilitates the growth of anatase from an amorphous phase. In the specific synthesis process for STP-2 and STP-4 we think that an amorphous TiO$_2$ phase is first created. Next, a peptization process occurs during the magnetic stirring (for 24 h), due to the acidic medium created by Ox, and this promotes the formation of anatase crystals observed by HREM (see Fig. 6). In the case of STP-1, the fast hetero-condensation of Si and Ti could prevent the peptization process. In addition, the pH value of the medium is lower due to the lower Ox concentration, preventing the peptization process, too.

Finally, the significant difference observed in the size of TiO$_2$ domains between STP-2 and STP-4 may be associated with their different Ox concentration. As Mahshid et al. reported [32], smaller and more spherical TiO$_2$ nanoparticles are created as pH is increased. As observed by TEM (Fig. 5), STP-4 (with the highest Ox concentration) presents the TiO$_2$ domains with the lowest size and the most spherical shape.

We investigated the surface topography of the materials under study, using AFM. Fig. 7a–c shows their 1 μm × 1 μm 2D top views. The corresponding 3D surface plots are shown in Fig. 7e–g. All materials consist of aggregates with morphology similar to that observed by TEM. The presence of an organic component (PDMS) in our materials could be responsible for the formation of roughness peaks on all the surfaces tested. As we previously discussed [14,15], this is a consequence of the elastic behavior of PDMS chains, which shrink greatly during the drying process of the gel network.

However, clear differences can be established in the roughness of the three materials under study. The materials with the highest Ox concentration (STP-2 and STP-4) present higher roughness values than that shown by STP-1. We associated this feature with the growth of TiO$_2$ nanoparticles in the SiO$_2$ matrix, promoting separate domains. The formation of separate domains (nanoclusters) in titania-silica samples, observed by AFM, has been reported previously [44,45]. In contrast, STP-1 (Fig. 7a and e) presents the lowest roughness value (5.1 nm) because the Si and Ti precursors are mixed at the atomic level, as previously discussed, and thus, these nanoclusters are not created. As reported in the previous paragraph, the roughness of STP-1 is attributed to the PDMS chains integrated in the matrix. Comparing STP-2 and STP-4, the images illustrate
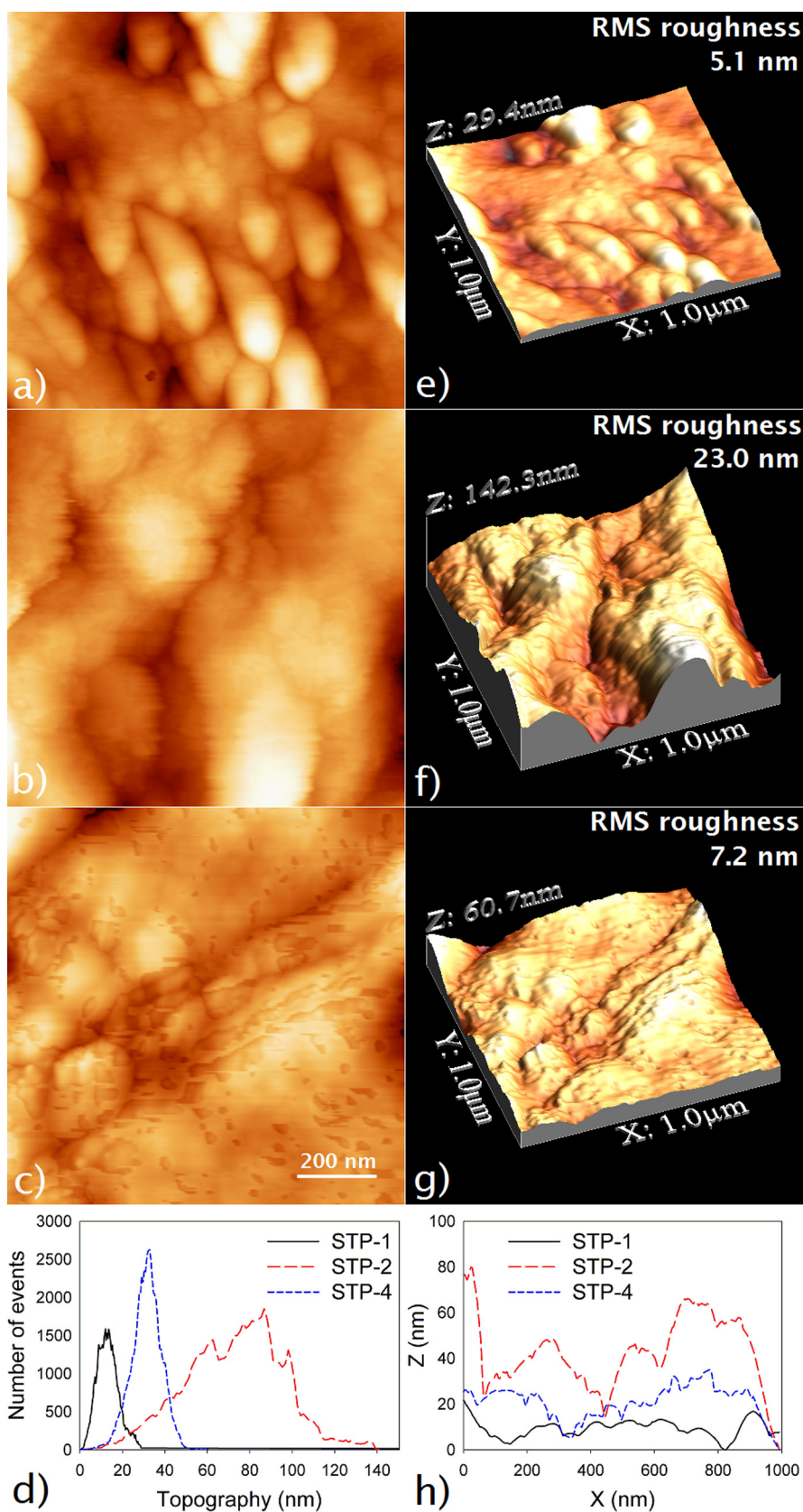
Fig. 7. (a–c) Images by 2D-AFM; (e–g) 3D-AFM of STP-1, STP-2 and STP-4, respectively; (d) particle size distribution (*Z*-axis) and (h) typical roughness profiles for the materials under study are also presented.
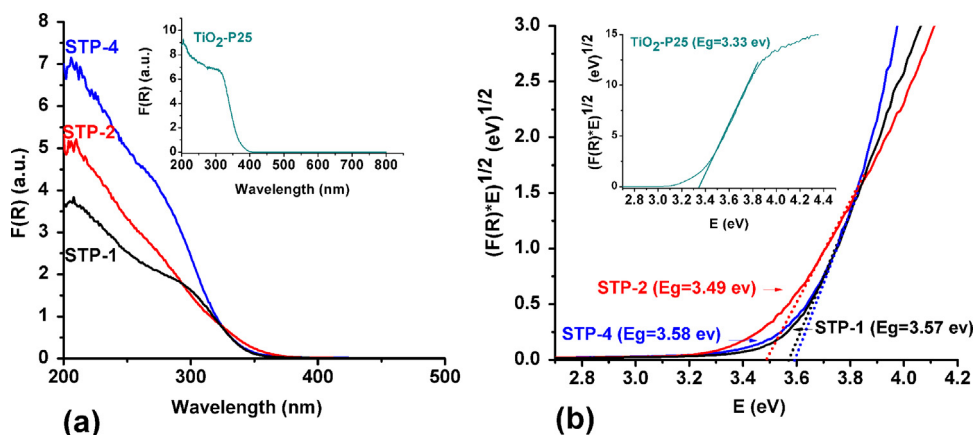
Fig. 8. (a) DR-UV–vis spectra and (b) plots of modified Kubelka–Munk: $(F(R)E)^{1/2}$ versus E of the nanocomposites. P25 plots are included in the corresponding insets.

that the material with the higher Ox concentration (STP-4, Fig. 7c and g) produces a surface of much lower roughness value (7.2 nm). We attribute this feature to the formation of TiO_2 nanoparticles of smaller size than those created in STP-2 (23.0 nm, see Fig. 7b and f). As previously established in the TEM discussion, particle size distribution presents lower values at lower pH levels [32].

Fig. 7d shows the height (Z) distribution across the surfaces of the three materials evaluated. STP-2 show a significantly broader Gaussian distribution than that found for the other two materials as a consequence of the presence of larger TiO_2 nanoparticles which raise the average roughness to higher values. STP-4 presents a higher average roughness than that associated with STP-1 due to the presence of TiO_2 nanoparticles, which are absent from STP-1. As an example of the roughness profiles obtained for the materials under study, one profile for each material is shown in Fig. 7h. These results are in good agreement with our previous AFM results corresponding to SiO_2 materials with embedded TiO_2 nanoparticles [45].

Fig. 8a illustrates the UV–vis diffuse reflectance spectra of the three nanocomposites under study together with the P25 spectrum in the inset. The values of energy gap (Eg) of these samples were obtained from the spectra illustrated in Fig. 8b by plotting $(F(R)E)^{1/2}$ versus E, according to the method proposed by Tandom

and Gupta [46]. It should be mentioned that the major component of the nanocomposites under study (SiO_2) does not absorb in the range of 200–800 nm. Therefore, the obtained absorptions refer to TiO_2. As expected, P25 (pure TiO_2) exhibits the lowest value of Eg (3.33 eV). Our nanocomposites exhibit higher values of Eg in the range of 3.49 up to 3.58 eV, as an effect of the presence of silica.

By comparing the three materials under study, the lowest band gap value was registered for STP-2. According to the literature [47,48], a semiconductor band gap is reduced as the crystal size is increased, according to the quantum size effect. Thus, the largest TiO_2 crystalline particle size of STP-2, observed by TEM (see Fig. 5), produces a decrease in band gap for this material. Regarding to the other two materials, similar band gap values were found. We want to notice that STP-1 presents absorption in the UV range in spite of the absence of independent domains of TiO_2 crystals. The UV absorption in amorphous and dispersed Ti integrated in titanium-silicon materials was previously reported [49].

3.2. Photocatalytic activity

The photocatalytic activity of the materials under study was evaluated by measuring the degradation of MO under UV–vis (see Fig. 9). The respective pseudo-first order rate constants are given
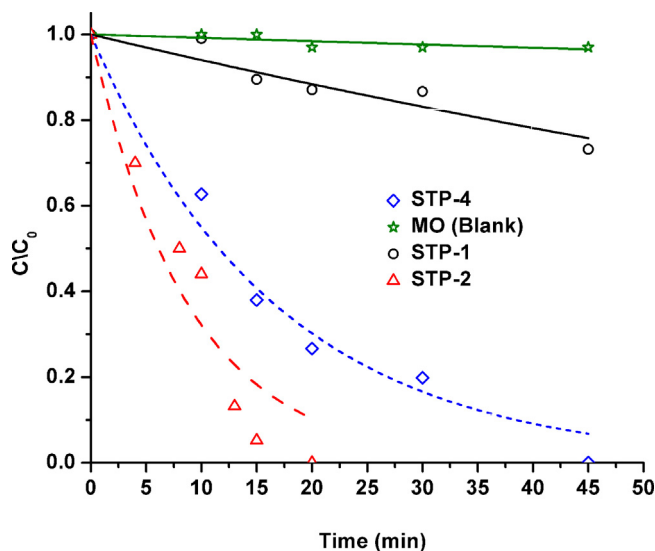

Fig. 9. Photocatalytic degradation of Methyl Orange (MO) in the presence of the nanocomposites under study. The curves represent the fitting of the pseudo-first order equation to the experimental data.
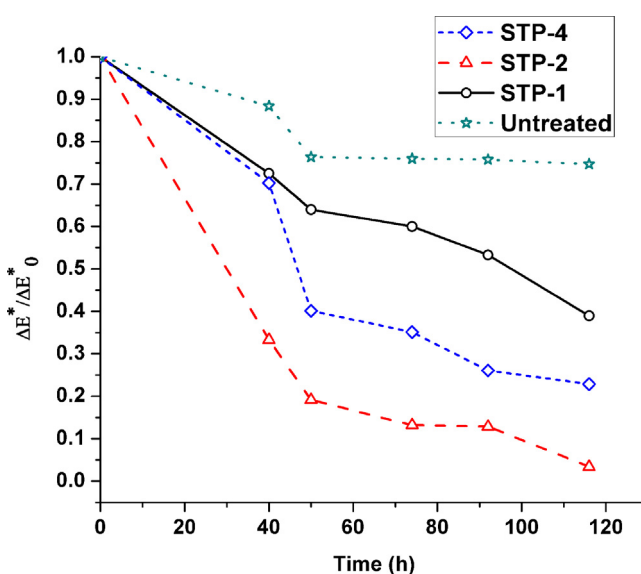

Fig. 10. Evolution of photocatalytic degradation of Methylene Blue (MB) on marble specimens treated with STP-1, STP-2 and STP-4, as well as the untreated specimen.

Table 3
Pseudo-first kinetic rate constant (k) and regression coefficient (r^2) of Methyl Orange degradation, under UV irradiation, in the presence of the nanocomposites under study.

Nano composite	k (10^{-3} min^{-1})	r^2
MO (blank)	0.8	0.91
STP-1	6	0.90
STP-2	113	0.92
STP-4	60	0.98

in Table 3. As observed in Fig. 9, the contribution of photochemical degradation for the elimination of MO is practically negligible. Comparing the activity of the materials prepared in our laboratory, it can be observed that STP-1 shows a significantly lower activity ($k = 6.2 \times 10^{-3}$ min^{-1}) than that observed for the STP-2 and STP-4 materials with higher Ox concentration (with kinetic rate constants 113×10^{-3} and 60×10^{-3} min^{-1}, respectively). These results suggest that Ox concentration may contribute to the photoactivity of these materials, by acting as a hole scavenger [19–22]. As we have already mentioned, the oxalic ions are good bidentate ligands and, at low pH values, they can be absorbed very strongly on the surfaces of TiO$_2$. In addition, the great efficiency of oxalic acid for the photocatalytic procedure can be also ascribed to its ability to produce CO$_2$•$^-$, as per the equation presented below as Eq. (2). The latter radicals might also have the ability either to directly decompose

the compounds or, through reaction with O$_2$, to enhance the production of O$_2$•$^-$/HO$_2$•, thus increasing the photoactivity [19–22]:

$$C_2O_4{}^{2-} + h^+ \rightarrow CO_2 + CO_2{}^{\bullet -} \tag{2}$$

The hole capturing from the oxalic ion allows the e$^-$ along with the oxidized radicals (CO$_2$•$^-$) to reductively decompose the MO. Studies taking in consideration the MO degradation in the presence of EDTA, which is another good bidentate ligand, proved that a significant photocatalytic enhancement was achieved upon the addition of EDTA [50].

In order to confirm the contribution of Ox to the photoactivity of the nanocomposites, we have evaluated the photoactivity of TiO$_2$ for the degradation of MO under UV–vis in the presence of Ox. We also carried out the same test without Ox. The results obtained, shown in the supplementary information (Fig. S5 and Table S1), indicate that Ox increases the photoactivity of TiO$_2$. This observation suggests that Ox could be improving the photoactivity of TiO$_2$ in our materials. On the other hand, the lower photoactivity of STP-1 could also be associated to the absence of crystalline TiO$_2$ phases [43] as separate domains [45]. If we further compare the photoactivity of the two materials with the highest Ox content, STP-2 presents a higher activity due to the contribution of a higher TiO$_2$ content present in separate domains and due to its larger crystal size, as we previously confirmed by TEM (Fig. 5) and UV-vis (Fig. 8). This increase in particle size generates a higher availability
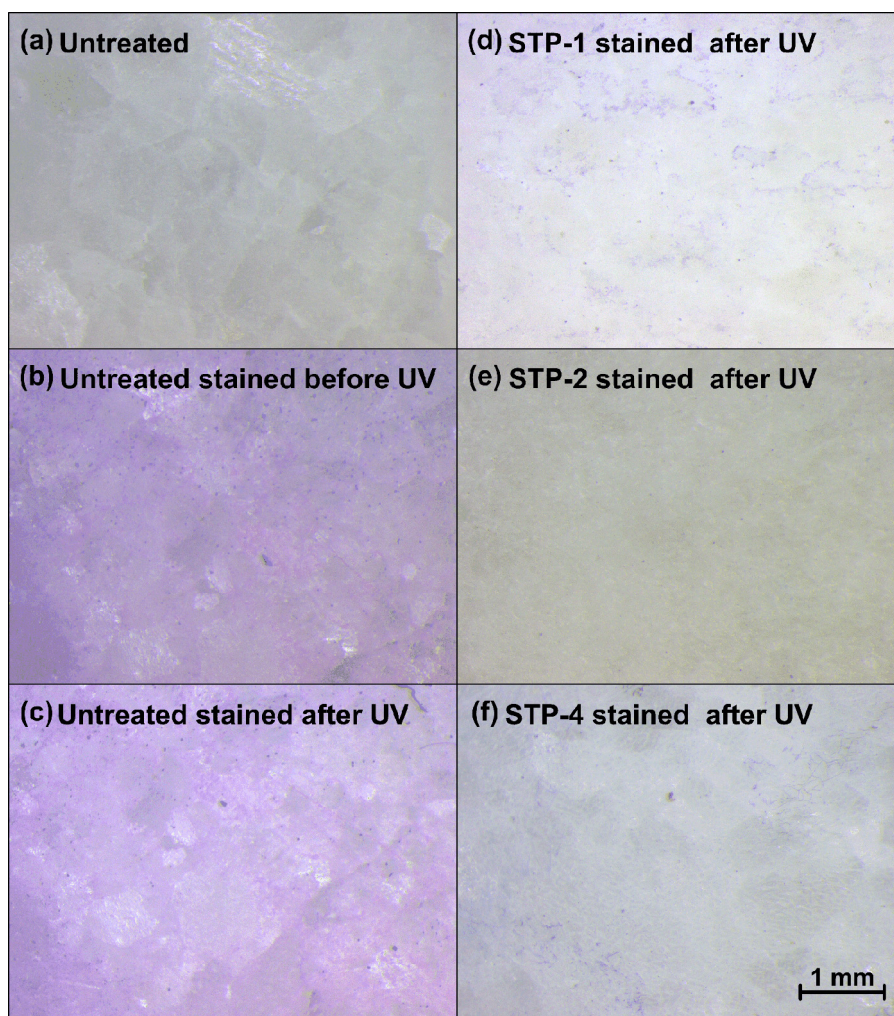

Fig. 11. Optical microscopy images of colored surfaces of the treated and untreated marbles before and after UV irradiation for 116 h. The images before UV irradiation correspond to: (a) untreated marble before MB staining, (b) untreated marble after MB staining. The images after 116 h of UV irradiation correspond to: (c) untreated marble; (d) marble treated with STP-1; (e) marble treated with STP-2; (f) marble treated with STP-4.

Table 4
Properties of the treated marble samples and their untreated counterparts.[a]

Sample	Untreated	Treated with STP-2	Treated with STP-4
Dry matter (mg cm^{-2})	–	0.4122 ± 0.0115	0.4237 ± 0.0418
ΔE^*	–	0.61 ± 0.05	1.88 ± 0.05
Contact angle (°)	56 ± 3	104 ± 2	95 ± 2
WCA (mg cm^{-2} s$^{-1/2}$)	0.0485 ± 0.0021	0.0059 ± 0.0003	0.0096 ± 0.0002
TWCA (%)	0.57 ± 0.04	0.30 ± 0.04	0.36 (±0.02)
WVP (g cm^{-2} h^{-1})	0.0040 ± 0.0003	0.0033 ± 0.0004	0.0031 ± 0.0002

[a] Data correspond to average values obtained from five measurements. Standard deviations are also included.

of photoactive sites for the degradation of MO under UV-vis, as van Grieken et al. [51] previously described. According to these authors, an optimal photoactivity could be obtained for TiO$_2$ particle sizes of around 6–7 nm, which are similar to those corresponding to STP-2. Shiba et al. [52] have also obtained the highest photoactivity for materials presenting the highest anatase crystal size.

3.3. Application of the nanocomposites on stone

The two nanocomposites showing faster MO photodegradation (STP-2 and STP-4) were brushed, as sols, on polished marble surfaces in order to assess their effectiveness as protective coatings. The dry matter values were similar for both nanocomposites (see Table 4).

The total color variation (ΔE^*) of samples after application of the treatments (Table 4) is below the perception threshold, for both products [6]. These results confirm that these nanocomposites can be employed as coatings without producing adverse esthetic modifications on the substrates.

The hydrophobic effectiveness of both nanocomposites was evaluated by means of contact angle measurements and the water capillary absorption test. The static contact angle (CA) values obtained (see Table 4) demonstrate that the two materials induce the hydrophobicity of the marble under study. This effect could be associated with the formation of an organic–inorganic hybrid coating due to the addition of PDMS to the starting sol. As previously described [14,15] this organic component reduces the surface energy, producing hydrophobicity. Comparing STP-2 and STP-4 values, the CA is higher for STP-2. Since these two products present the same PDMS content the difference in CA could be attributed to the higher roughness value observed for STP-2 (Fig. 7) [14].

The results obtained from the capillary absorption test confirm both the hydrophobic behavior and the differences observed between the coatings. Specifically, water capillary absorption coefficients (WCA) were decreased by 88 and 80% for STP-2 and STP-4, respectively. The total amount of capillary absorbed water (TWCA) decreased by 47 and 37%, respectively (see Table 4).

Regarding the vapor permeability test, the water vapor coefficients (WVP) decreased by approximately 18 and 23% for STP-2 and STP-4, respectively (see Table 4). These reductions comply with the acceptable ranges for building materials [15].

The results of the photocatalytic test carried out on marble samples are shown in Fig. 10, where the obtained ratios of $\Delta E^*/\Delta E_0^*$ at various times are illustrated. The results match perfectly those obtained from the photocatalytic test of the nanocomposite. Untreated samples showed a slight MB degradation due to a photochemical mechanism [53]. The marble samples treated with STP-1 showed a significantly slower degradation profile associated with the absence of separate TiO$_2$ domains in the coating. Faster degradation of MB was observed for marble treated with STP-2 and STP-4. As previously described, this very high activity can be attributed to the mentioned presence of TiO$_2$ in separate domains for these two materials. Comparing these two materials, the higher activity of the STP-2-treated marble samples can be attributed to the larger anatase crystal size and the presence a greater amount of crystals,

as observed by TEM. The optical microscopy images of the photocatalytic experiments of MB applied to treated and untreated marble surfaces are shown in Fig. 11. These images further confirm that STP-2 presents the better photocatalytic behavior, since the most effective color removal has been observed on the marble treated with STP-2 (Fig. 11e). The decomposition of MB is mainly due to the oxidation induced by the presence of TiO$_2$. Ox could favor this process [54]. These results confirm the effectiveness of these novel nanomaterials as self-cleaning agents.

4. Conclusions

We have designed an innovative and simple synthesis route for producing photoactive, transparent and hydrophobic SiO$_2$-crystalline TiO$_2$ nanocomposites for application on stone. We have also demonstrated that these nanocomposites produce photoactive and hydrophobic coatings when applied, as sols, brushed onto stone. Thus, they are expected to find commercial applications as protective coatings of building materials, since they meet user requirements for a self-cleaning and hydrophobic product that preserves the esthetic qualities of stone.

This new route consists of mixing titanium and silicon alkoxides in the presence of oxalic acid. An organic silica oligomer is also added to reduce surface energy, and subsequently to give hydrophobic properties to the material. In this synthesis route, oxalic acid plays a key role: (1) by promoting the simultaneous sol–gel transition for titanium and silicon alkoxides, through its role as a chelating agent which delays the hydrolysis of the titanium precursor; (2) by producing anatase crystals at ambient temperature through a peptization process, which occurs in an acidic medium created by Ox; (3) by increasing the nanocomposite photoactivity by acting as a hole-scavenger; (4) by creating a crack-free material due to its effect as a DCCA; and (5) by acting as a sol–gel catalyst.

From our investigation of the microstructure of these photocatalysts, we conclude that the formation of independent domains of TiO$_2$ inside the SiO$_2$ matrix, and the formation of anatase of a suitable crystal size, are both essential factors for improving the photoactivity of the nanocomposites. We also conclude that oxalic acid concentration plays a crucial role for the formation of this optimum structure.

Appendix A. Supplementary data

Supplementary data associated with this article can be found, in the online version, at http://dx.doi.org/10.1016/j.apcatb.2014.03.042.

References

[1] I. Karastasios, M.S. Katsiotis, V. Likodimos, A. Kontos, G. Papavassiliou, P. Falaras, V. Kilikoglou, Appl. Catal. B: Environ. 95 (2010) 78–86.
[2] M. Lackhoff, X. Prieto, N. Nestle, F. Dehn, R. Niessner, Appl. Catal. B: Environ. 43 (2003) 205–216.
[3] P. Maravelaki-Kalaitzaki, Z. Agioutantis, E. Lionakis, M. Stavroulaki, V. Perdikatsis, Cem. Concr. Compos. 36 (2013) 33–41.
[4] L. Pinho, M.J. Mosquera, J. Phys. Chem. C 115 (2011) 22851–22862.
[5] L. Pinho, F. Elhaddad, D.S. Facio, M.J. Mosquera, Appl. Surf. Sci. 275 (2013) 389–396.
[6] L. Pinho, M.J. Mosquera, Appl. Catal. B: Environ. 134–135 (2013) 205–221.
[7] I. Poulios, P. Spathis, A. Grigoriadou, K. Delidou, P. Tsoumparis, J. Environ. Sci. Health A 34 (1999) 1455–1471.
[8] E. Quagliarini, F. Bondioli, G. Goffredo, C. Cordoni, P. Munafò, Constr. Build. Mater. 37 (2012) 51–57.
[9] M.F. La Russa, S.A. Ruffolo, N. Rovella, C.M. Belfiore, A.M. Palermo, M.T. Guzzi, G.M. Crisci, Prog. Org. Coat. 74 (2012) 186–191.
[10] L. Bergamonti, I. Alfieri, A. Lorenzi, A. Montenero, G. Predieri, G. Barone, P. Mazzoleni, S. Pasquale, P.P. Lottici, Appl. Surf. Sci. 282 (2013) 165–173.
[11] A. Pénard, T. Gacoin, J. Boilot, Acc. Chem. Res. 40 (2007) 895–902.
[12] R. Davis, Z. Liu, Chem. Mater. 9 (1997) 2311–2324.
[13] C. Kapridaki, P. Maravelaki-Kalaitzaki, Prog. Org. Coat. 76 (2013) 400–410.
[14] J.F. Illescas, M.J. Mosquera, J. Phys. Chem. C 115 (2011) 14624–14634.
[15] J.F. Illescas, M.J. Mosquera, ACS Appl. Mater. Interfaces 4 (2012) 4259–4269.
[16] V. Fassina, Sci. Total Environ. 167 (1995) 185–203.
[17] P. Maravelaki-Kalaitzaki, Anal. Chim. Acta 532 (2005) 187–198.
[18] L.L. Hench, in: L.L. Hench, D.R. Ulrich (Eds.), Science of Ceramic Chemical Processing, Wiley-Interscience, 1986, p. 52.
[19] Y. Wang, P. Zhang, J. Hazard. Mater. 192 (2011) 1869–1875.
[20] Y. Li, F. Wasgestian, J. Photochem. Photobiol. A 112 (1998) 255–259.
[21] S. Bassaid, D. Robert, M. Chain, Appl. Catal. B: Environ. 86 (2009) 93–97.
[22] W. Gao, R. Jin, J. Chen, X. Guan, H. Zeng, F. Zhang, N. Guan, Catal. Today 90 (2004) 331–336.
[23] G. Fu, P.S. Vary, C. Lin, J. Phys. Chem. B 109 (2005) 8889–8898.
[24] M. Thommes, B. Smarsly, M. Groenewolt, P.I. Ravikovitch, A.V. Neimark, Langmuir 22 (2006) 756–764.
[25] L.M. Pastrana-Martínez, S. Morales-Torres, S.K. Papageorgiou, F.K. Katsaros, G.E. Romanos, J.L. Figueiredo, J.L. Faria, P. Falaras, A.M.T. Silva, Appl. Catal. B: Environ. 142–143 (2013) 101–111.
[26] UNI EN 15801:2010, Conservation of Cultural Property—Test Methods—Determination of water absorption by capillarity, Official Italian version of EN 15801:2009, European Standard issued by CEN, technical body CEN/TC 346 – Conservation of cultural property, Date of availability (DAV), 2009.
[27] D.S. Facio, M.J. Mosquera, ACS Appl. Mater. Interfaces 5 (2013) 7517–7526.
[28] UNI EN 15803:2010, Conservation of Cultural Property—Test Methods—Determination of water vapour permeability (dp), Official Italian version of EN 15803:2009 European Standard issued by CEN, technical body CEN/TC 346 – Conservation of cultural property, Date of availability (DAV), 2009.
[29] R.S. Berns, Billmeyer and Saltzman's Principles of Color Technology, Wiley-Interscience, New York, 2000.
[30] H.S. Kibombo, R. Pey, S. Rasalingam, R.T. Koodali, Catal. Sci. Technol. 2 (2012) 1737–1766.
[31] S. Doeuff, M. Henry, C. Sanchez, J. Livage, J. Non-Cryst. Solids 89 (1987) 206–216.
[32] S. Mahshid, M. Askari, M. Sasani Ghamsari, J. Mater. Synth. Process. 189 (2007) 296–300.
[33] L. Téllez, J. Rubio, F. Rubio, E. Morales, J.L. Oteo, Spectrosc. Lett. 37 (2004) 11–31.
[34] T. Lopez, E. Sanchez, P. Bosch, Y. Meas, R. Gomez, Mater. Chem. Phys. 32 (1992) 141–152.
[35] P.D. Moran, G.A. Bowmaker, R.P. Cooney, K.S. Finnie, J.R. Bartlett, J.L. Woolfrey, Inorg. Chem. 37 (1998) 2741–2748.
[36] P. Novotna, J. Zita, G. Krysa, V. Kalousek, J. Rathousky, Appl. Catal. B: Environ. 79 (2007) 179–185.
[37] M. Kruk, M. Jaroniec, Chem. Mater. 13 (2001) 3169–3183.
[38] X. Gao, I.E. Wachs, Catal. Today 51 (1999) 234–254.
[39] D.S. Gopala, R.R. Bhattacharjee, R. Haerr, B. Yeginoglu, O.D. Pavel, B. Cojocaru, V.I. Parvulescu, R.M. Richards, Chem. Cat. Chem. 3 (2011) 408–416.
[40] J.M. Thomas, P.A. Midgley, T.J.V. Yates, J.S. Barnard, R. Raja, I. Arslan, M. Weylan, Angew. Chem. Int. Ed. 43 (2004) 6745–6747.
[41] M. Bonne, S. Pronier, Y. Battonneau, F. Can, X. Courtois, S. Royer, P. Marécot, D. Duprez, J. Mater. Chem. 20 (2010) 9205–9214.
[42] H. Shin, H.S. Jung, K.S. Hong, J.K. Lee, Catal. Lett. 33 (2004) 1382–1383.
[43] B. Fei, Z. Deng, J.H. Xin, Y. Zhang, G. Pang, Nanotechnology 17 (2006) 1927–1931.
[44] Y.V. Lim, H. Fan, Z. Shen, C.H. Kang, Y. Feng, S. Wang, Appl. Phys. A 95 (2009) 555–562.
[45] L. Pinho, J.C. Hernandez-Garrido, J.J. Calvino, M.J. Mosquera, Phys. Chem. Chem. Phys. 15 (2013) 2800–2808.
[46] S.P. Tandon, J.P. Gupta, Phys. Status Solidi 38 (1970) 363–367.
[47] B. Llano, M.C. Hidalgo, L.A. Rios, J.A. Navío, Appl. Catal. B: Environ. 150–151 (2014) 389–395.
[48] H. Dimitroula, V.M. Daskalaki, Z. Frontistis, D.I. Kondarides, P. Panagiotopoulou, N.P. Xekoukoulotakis, D. Mantzavinos, Appl. Catal. B 117–118 (2012) 283–291.
[49] H. Yamashita, S. Kawasaki, Y. Ichihashi, M. Harada, M. Takeuchi, M. Anpo, G. Stewart, M.A. Fox, C. Louis, M. Che, J. Phys. Chem. B 102 (1998) 5870–5875.
[50] L.M. Pastrana-Martínez, S. Morales-Torres, A.G. Kontos, N.G. Moustakas, J.L. Faria, J.M. Doña-Rodríguez, P. Falaras, A.M.T. Silva, Chem. Eng. J. 224 (2013) 17–23.
[51] R. van Grieken, J. Aguado, M.J. López-Muñoz, J. Marugán, J. Photochem. Photobiol. A 148 (2002) 315–322.
[52] K. Shiba, S. Sato, M. Ogawa, J. Mater. Chem. 22 (2012) 9963–9969.
[53] A. Mills, J. Wang, J. Photochem. Photobiol. A: Chem. 127 (1999) 123–134.
[54] A. Pandikumar, R. Ramaraj, J. Hazard. Mater. 203–204 (2012) 244–250.